J. Fluid Mech. (2002), *vol.* 459, *pp.* 43–65.
DOI: 10.1017/S0022112002008108 Printed in the United Kingdom

The trajectory and stability of a spiralling liquid jet. Part 1. Inviscid theory

By I. M. WALLWORK[1], S. P. DECENT[1], A. C. KING[1] AND R. M. S. M. SCHULKES[2]

[1]School of Mathematics and Statistics, The University of Birmingham, Edgbaston, Birmingham, B15 2TT, UK

[2]Norsk Hydro a.s., Research Centre Porsgrunn, N-3901 Porsgrunn, Norway

(Received 9 May 2001 and in revised form 24 August 2001)

We examine a spiralling slender inviscid liquid jet which emerges from a rapidly rotating orifice. The trajectory of this jet is determined using asymptotic methods, and the stability using a multiple scales approach. It is found that the trajectory of the jet becomes more tightly coiled as the Weber number is decreased. Unstable travelling wave modes are found to grow along the jet. The breakup length of the jet is calculated, showing good agreement with experiments.

1. Introduction

In this paper we present an asymptotic method to determine the trajectory and linear stability of a slender jet with a curved centreline. We concentrate on the problem of an inviscid jet, subject to surface tension forces, which is ejected from a small hole in a rotating container. This problem arises in the manufacture of pellets using the prilling process. Here hot liquid jets emerge from a rotating container and break up into droplets due to a surface-tension-driven instability. The jets do not fall significantly under gravity before they break up into droplets. After breakup the droplets then fall under gravity where they solidify and form into pellets. See figure 1 (Andersen & Yttri 1997) for a photograph of jets in a typical prilling process, with figure 2 showing the position of the container on the photograph.

The first significant work on the free surface flow of liquid jets is that of Lord Rayleigh (1878). Rayleigh analysed the linear stability of an infinitely long, inviscid, incompressible liquid jet with circular cross-section that was subjected to disturbances from its equilibrium. He looked for travelling wave modes of the form $\exp(\mathrm{i}kx + \alpha t)$, where x is distance along the jet in the direction of the steady mean flow, t is time, k is the wavenumber, $\mathrm{Re}(\alpha)$ is the growth rate and $\mathrm{Im}(\alpha)$ is the (negative) frequency. Rayleigh showed that the unstable nature of liquid jets is caused by the surface tension force acting on the jet. He found that spatially harmonic disturbances of the radius grow in time according to

$$\alpha^2 = \left(\frac{\sigma}{\rho a^3}\right)\left(\frac{I_s'(ka)(1 - s^2 - k^2a^2)ka}{I_s(ka)}\right), \tag{1.1}$$

where ρ is the density, a the undisturbed radius, σ surface tension and I_s modified Bessel function of order s, where the integer $s \geqslant 0$ represents the periodicity of the motion around the cylindrical jet's circumference. This result predicts that for $s = 0$ the jet is stable for $ka > 1$ and unstable for $0 < ka < 1$. The jet is neutrally stable for

FIGURE 1. Photograph of jets emerging from a rotating container in prilling. The dark segment at the bottom of the photograph is an upper view of the rotating cylindrical container, which is rotating anticlockwise. Hundreds of jets can be seen, each emerging from small holes on the curved face of the cylinder. Some droplets, arising from jet breakup, can be observed too. The jet is seen to break up at a distance from the cylinder of the order of a hundred times the radius of a hole.

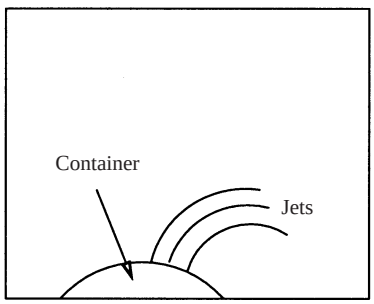

FIGURE 2. Diagram showing the position of the container on figure 1.

$s \geqslant 1$. By maximizing expression (1.1), the maximum value of the growth rate was found to be associated with $ka = 0.697$.

It is generally accepted that Rayleigh's inviscid linear model describes the beginning of liquid jet breakup. Weber (1931) introduced viscosity into the stability analysis and found that the most unstable wave was moved to longer wavelengths. A significant review of the early work on liquid jets is given by Bogy (1979) and a more up to date and extensive review is given by Eggers (1997). Other sources include the books by Middleman (1995) and Anno (1977).

Keller & Weitz (1957) looked at a two-dimensional steady sheet of liquid in order to study how the trajectory of a jet is affected when surface tension is included. They found that including surface tension had the effect of making the sheets fall more

sharply than with no surface tension. They found that for $We < 1$ the sheets rise instead of fall.

Keller & Geer (1973) looked at flows of thin streams of water with any type of free or solid boundary. They developed an asymptotic method using the slenderness of the stream to determine thin steady two-dimensional flows under the effects of gravity. Tuck (1976) determined the shape of a slender jet of water falling under gravity (without surface tension). He considered a vertically falling jet with the dominant velocity component in the vertical direction, and a curved jet that initially rises to a peak before falling under gravity. The trajectory of this curved liquid jet was found to be ballistic because surface tension was neglected. This study was restricted to jets with elliptic cross-sections and produced results that agreed with the work of Keller & Geer (1973) for a two-dimensional sheet of water.

Spatial instability of liquid jets was first considered by Keller, Rubinow & Tu (1973). Their key idea was that all jets really start from a nozzle. They therefore considered the instability of a circular cylindrical jet of liquid in still air under the assumption that the wavenumber k of the disturbance is complex, while α is purely imaginary. This means that the travelling wave disturbance grows with distance along the jet. (In temporal instability, the wavenumber k is real and α is complex.) In their analysis Keller *et al.* found that there are infinitely many unstable modes. They also found that the spatial modes of the liquid jet are related to Rayleigh's temporal modes for high-speed jets. This explains why Rayleigh and others found good agreement between their results and experimental data.

Liquid jets that leave an orifice and come into contact with air are known to break up into droplets. The sizes of the drops that are produced are of great interest in a variety of industrial processes, such as the injection of fuel into jet engines, the production of miniature spherical nuclear fuel particles by the Sol-Gel process and the production of fertiliser pellets by prilling. The early analytical work performed on liquid jets predicted the formation of only one droplet for a given disturbance wavelength. However experimental observations and more recent studies have found that two droplets are formed (see Chaudhary & Maxworthy 1980*a*, *b*; Donnelly & Glaberson 1966; Goedde & Yuen 1970). These are a main droplet and a smaller satellite droplet. The size of these droplets is affected by the perturbation wavelengths and magnitudes, and the Weber number.

Baird & Davidson (1962) looked at straight annular liquid jets where gravitational effects were neglected. They found a singularity at $We = 1$. Their equations are only accurate for long, fast annular jets. They found fair agreement with experiments. However, for very short jets agreement was not found. They concluded that this was due to the jet having relatively large menisci at the base, which would probably affect the jet profile. Finnicum, Weinstein & Ruschak (1993) studied two-dimensional liquid curtains falling under gravity. They found that the singularity at $We = 1$ is removable and indicates that the fluid leaves the nozzle with an angle which is different from the nozzle exit angle. For $We > 1$ a jet is always formed regardless of the angle at which the fluid leaves the nozzle. However, when $We < 1$ this angle is found to be crucial. Ramos (1996) studied a one-dimensional hydraulic model for inviscid incompressible axisymmetric annular liquid jets. He found that a long-wavelength approximation may not be valid for small Weber numbers. He also found for $We < 1$ the jet takes odd shapes; again the long-wavelength approximation may no longer be valid. The long-wavelength approximation is also not valid near the exit point. The occurrence of this singularity is still an unresolved issue.

The work of Hilbing & Heister (1996) examines in some detail the nonlinear in-

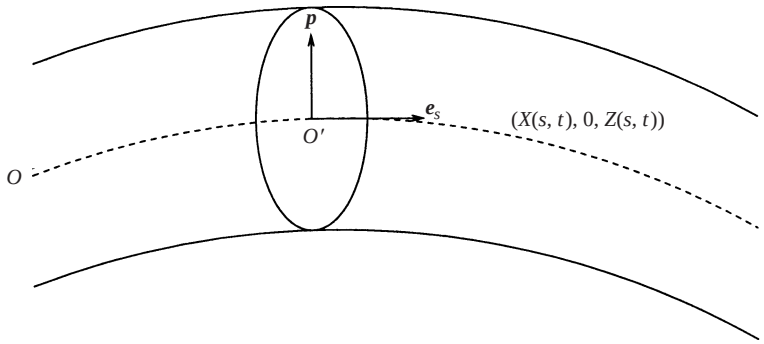

FIGURE 3. Sketch of a curved jet in the (X, Z)-plane.

stability of a straight jet. A boundary element method was used to investigate the nonlinear evolution of a straight liquid jet emerging from an orifice, in the absence of gravity, up to the point of pinch-off. They predict the size and formation of both main and satellite drops, taking into account the effects of velocity perturbations, wavenumbers and Weber number. They found encouraging agreement with experiments. Schulkes (1993) derived the one-dimensional nonlinear equations of motion governing axisymmetric long-wavelength disturbances of a straight inviscid liquid jet. He found exact periodic solutions to his equations, but these solutions only exist for wavenumbers where the long-wavelength approximation is not applicable. He looked at the numerical solutions of the nonlinear equations for the unstable case and concluded that satellite droplets are always formed.

This paper considers the problem of determining the trajectory and stability of a thin inviscid liquid jet that emerges from a rotating orifice. The viscous case will be the subject of a separate paper. We will determine the trajectory and stability of a jet emerging into a low-density fluid, so that the aerodynamic interference of air with the jet can be neglected. We start by defining a suitable coordinate system to describe the jet's surface and centreline, and determine the equations of motion in this coordinate system. Section 3 looks at the various steady solutions to our jet equations and what effect surface tension and rotation have on the position of the jet's centreline and cross-section. In §§ 4 and 5 the stability of the jet is analysed by a linear stability argument, using temporal and spatial stability methods respectively. Section 6 looks at experimental evidence of liquid jets. A series of experiments was performed to see how altering various parameters affects the trajectory, stability and droplet formation of the jet. We then compare the theoretical predictions with the experiments.

2. The equations of motion

An inviscid liquid jet leaves a small orifice of radius a situated on the curved face of a circular cylindrical container of radius s_0 which is rotating at a constant rate Ω about the axis of the cylinder. To describe this problem we choose a coordinate system (x, y, z) which rotates with the container, having its origin at the axis of the container, with the orifice positioned at $(s_0, 0, 0)$. If $s_0\Omega^2 >> g$ (where g is the acceleration due to gravity, where gravity acts in the direction of the negative y-axis) we will have a rapidly rotating jet in which fluid is moving mainly in the plane perpendicular to the axis of rotation (x, z-plane), and will consequently neglect the effects of the gravitational body force (setting $g = 0$).

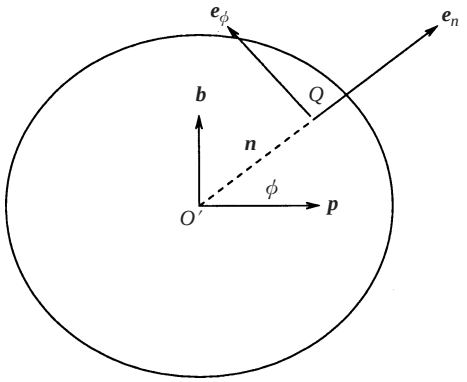

FIGURE 4. Cross-section of a curved jet.

An orthogonal coordinate system is needed in which we can conveniently describe the jet. One coordinate of this system will be the arclength s along the centreline of the jet. In any cross-section of the jet we also have plane polar coordinates in the radial and azimuthal directions (n, ϕ). These coordinates have unit vectors denoted by $\boldsymbol{e}_s, \boldsymbol{e}_n$ and $\boldsymbol{e}_\phi$ respectively, and are shown in figures 3 and 4.

The centreline of the jet (in the x, y, z-coordinate system) is described by $(X(s,t) + s_0, 0, Z(s,t))$. The unit vectors in this coordinate system are calculated using a principal normal vector $\boldsymbol{p}$ and a binormal vector $\boldsymbol{b}$ to the centreline (shown in figure 4). The position vector of any particle Q relative to the orifice O is

$$\boldsymbol{r} = \int_0^s \boldsymbol{e}_s \, \mathrm{d}s + n\boldsymbol{e}_n, \tag{2.1}$$

where s is the arclength and n a radial distance. It is straightforward to show that these form an orthogonal coordinate system (e.g. $\boldsymbol{e}_n \cdot \boldsymbol{e}_\phi = -Z_s^2 \cos\phi \sin\phi + \sin\phi \cos\phi - X_s^2 \cos\phi \sin\phi = 0$, as $X_s^2 + Z_s^2 = 1$).

The dynamics of the jet are described by the continuity equation, Euler's equations, the kinematic condition on the free surface, the pressure condition on the free surface, an arclength condition $X_s^2 + Z_s^2 = 1$ and $v = w = 0$ on $n = 0$, where $\boldsymbol{u} = u\boldsymbol{e}_s + v\boldsymbol{e}_n + w\boldsymbol{e}_\phi$ is the velocity field. We non-dimensionalize these equations using the following scalings:

$$\left.\begin{aligned} &\bar{u} = \frac{u}{U}, \quad \bar{v} = \frac{v}{U}, \quad \bar{w} = \frac{w}{U}, \quad \bar{p} = \frac{p}{\rho U^2}, \quad \bar{n} = \frac{n}{a}, \quad \epsilon = \frac{a}{s_0}, \\ &\bar{R} = \frac{R}{a}, \quad \bar{s} = \frac{s}{s_0}, \quad \bar{t} = \frac{tU}{s_0}, \quad \bar{X} = \frac{X}{s_0}, \quad \bar{Z} = \frac{Z}{s_0}, \end{aligned}\right\} \tag{2.2}$$

where U is the exit speed of the jet, R is the radius of the jet, p is the pressure and ϵ is the aspect ratio. Substituting these scalings into our dynamical equations (these can be found in Wallwork 2001 as they are too lengthy to give here), with due account being taken of the motion of the unit vectors (and dropping overbars for simplicity of notation), we obtain the conservation of mass

$$\epsilon n \frac{\partial u}{\partial s} + (1 + \epsilon n \cos\phi (X_s Z_{ss} - X_{ss} Z_s)) \left(v + n \frac{\partial v}{\partial n} + \frac{\partial w}{\partial \phi} \right) + \epsilon n (X_s Z_{ss} - X_{ss} Z_s)(v \cos\phi - w \sin\phi) = 0, \tag{2.3}$$

Euler's equations

$$\begin{aligned}(1+\epsilon n\cos\phi(X_sZ_{ss}-X_{ss}Z_s))&\left(\epsilon\frac{\partial u}{\partial t}+\epsilon u(X_{st}X_s-Z_{st}Z_s)\right.\\&\left.+\epsilon v\cos\phi(Z_{st}X_s-X_{st}Z_s)+\epsilon w\sin\phi(X_{st}Z_s-Z_{st}X_s)+v\frac{\partial u}{\partial n}+\frac{w}{n}\frac{\partial u}{\partial\phi}\right)\\&+\epsilon u\frac{\partial u}{\partial s}+\epsilon u(X_sZ_{ss}-X_{ss}Z_s)(v\cos\phi-w\sin\phi)\\=&-\epsilon\frac{\partial p}{\partial s}+\left(\frac{2\epsilon}{Rb}(v\cos\phi-w\sin\phi)+\frac{\epsilon}{Rb^2}((X+1)X_s+ZZ_s)\right)\\&\times(1+\epsilon n\cos\phi(X_sZ_{ss}-X_{ss}Z_s)),\end{aligned}\tag{2.4}$$

$$\begin{aligned}(1+\epsilon n\cos\phi(X_sZ_{ss}-X_{ss}Z_s))&\left(\epsilon\frac{\partial v}{\partial t}+\epsilon u\cos\phi(X_{st}Z_s-Z_{st}X_s)\right.\\&-\frac{w}{n}\sin\phi(Z_sX_t-X_sZ_t)+\epsilon v\cos^2\phi(X_{st}X_s+Z_{st}Z_s)\\&\left.-\epsilon w\cos\phi\sin\phi(X_{st}X_s+Z_{st}Z_s)+v\frac{\partial v}{\partial n}+\frac{w}{n}\frac{\partial v}{\partial\phi}-\frac{w^2}{n}\right)\\&+\epsilon u\frac{\partial v}{\partial s}-\epsilon\cos\phi(X_sZ_{ss}-X_{ss}Z_s)u^2\\=&\left(-\frac{\partial p}{\partial n}-\frac{2\epsilon}{Rb}u\cos\phi+\frac{\epsilon\cos\phi}{Rb^2}((X+1)Z_s-ZX_s+\epsilon n\cos\phi)\right)\\&\times(1+\epsilon n\cos\phi(X_sZ_{ss}-X_{ss}Z_s)),\end{aligned}\tag{2.5}$$

$$\begin{aligned}(1+\epsilon n\cos\phi(X_sZ_{ss}-X_{ss}Z_s))&\left(\epsilon\frac{\partial w}{\partial t}+\epsilon u\sin\phi(Z_{st}X_s-X_{st}Z_s)\right.\\&+\frac{v}{n}\sin\phi(Z_sX_t-X_sZ_t)-\epsilon v\cos\phi\sin\phi(X_{st}X_s+Z_{st}Z_s)\\&\left.+\epsilon w\sin^2\phi(X_{st}X_s+Z_{st}Z_s)+v\frac{\partial w}{\partial n}+\frac{w}{n}\frac{\partial w}{\partial\phi}+\frac{vw}{n}\right)\\&+\epsilon u\frac{\partial w}{\partial s}+\epsilon\sin\phi(X_sZ_{ss}-X_{ss}Z_s)u^2\\=&\left(-\frac{1}{n}\frac{\partial p}{\partial\phi}+\frac{2\epsilon}{Rb}u\sin\phi+\frac{\epsilon\sin\phi}{Rb^2}(ZX_s-(X+1)Z_s-\epsilon n\cos\phi)\right)\\&\times(1+\epsilon n\cos\phi(X_sZ_{ss}-X_{ss}Z_s)),\end{aligned}\tag{2.6}$$

the kinematic condition

$$(1+\epsilon n\cos\phi(X_sZ_{ss}-X_{ss}Z_s))\left(\epsilon\frac{\partial R}{\partial t}+(Z_sX_t-X_sZ_t)\cos\phi+\frac{w}{n}\frac{\partial R}{\partial\phi}-v\right)+\epsilon u\frac{\partial R}{\partial s}=0 \quad \text{on } n=R,\tag{2.7}$$

the pressure condition

$$p=\frac{\kappa}{We}\quad\text{on } n=R,\tag{2.8}$$

where

$$\kappa = \frac{1}{h}\left(\epsilon^2 \frac{\partial}{\partial s}\left(-\frac{1}{hE}\frac{\partial R}{\partial s}\right) + \frac{1}{n}\frac{\partial}{\partial n}\left(\frac{nh}{E}\right) + \frac{\partial}{\partial \phi}\left(-\frac{h}{n^2 E}\frac{\partial R}{\partial \phi}\right)\right) \tag{2.9}$$

is the curvature,

$$h = 1 + \epsilon n \cos\phi (X_s Z_{ss} - X_{ss} Z_s), \tag{2.10}$$

$$E = \left(1 + \frac{\epsilon^2}{h^2}\left(\frac{\partial R}{\partial s}\right)^2 + \frac{1}{n^2}\left(\frac{\partial R}{\partial \phi}\right)^2\right)^{1/2}, \tag{2.11}$$

the arclength condition

$$X_s^2 + Z_s^2 = 1 \tag{2.12}$$

and

$$v = w = 0 \quad \text{on } n = 0, \tag{2.13}$$

where $Rb = U/s_0\Omega$ is the Rossby number and $We = \rho\, U^2 a/\sigma$ is the Weber number. The Rossby number represents a balance between inertia and rotational forces and the Weber number the balance between inertia and surface tension forces.

Equations (2.3)–(2.13) now give us a full set of expressions that represent the behaviour of the curved jet. In the following sections we present a steady asymptotic solution, based on small ϵ, which is of relevance to the prilling process.

3. Asymptotic form of steady-state solutions

We will consider the case where the jet leaves the orifice projected in a direction normal to the surface of the cylindrical container in the rotating frame, with speed U. The exit radius of the jet is taken to be the radius of the orifice a. In non-dimensional variables this gives $X_s = 1, X = Z = Z_s = 0, R_0 = u_0 = 1$ at $s = 0$. Asymptotic expansions for u, v, p, R, X and Z are introduced and we simplify by considering flow without azimuthal rotation, i.e. $w = 0$. We look for a slender liquid jet where the velocity and pressure gradient are parallel to the centreline at leading order. We therefore use the steady expansions

$$u = u_0(s) + \epsilon u_1(s, n, \phi) + \cdots, \tag{3.1}$$

$$v = \epsilon v_1(s, n, \phi) + \epsilon^2 v_2(s, n, \phi) + \cdots, \tag{3.2}$$

$$p = p_0(s, n, \phi) + \epsilon p_1(s, n, \phi) + \cdots, \tag{3.3}$$

$$R = R_0(s) + \epsilon R_1(s, \phi) + \cdots, \tag{3.4}$$

$$X = X_0(s) + \epsilon X_1(s) + \cdots, \tag{3.5}$$

$$Z = Z_0(s) + \epsilon Z_1(s) + \cdots, \tag{3.6}$$

and then substitute these series into equations (2.3)–(2.13) (note that we write X_0 and Z_0 as X and Z respectively for simplicity) to obtain the following sequence of equations:

$$n\frac{\mathrm{d}u_0}{\mathrm{d}s} + v_1 + n\frac{\partial v_1}{\partial n} = 0, \tag{3.7}$$

$$u_0\frac{\mathrm{d}u_0}{\mathrm{d}s} = -\frac{\partial p_0}{\partial s} + \frac{1}{Rb^2}((X+1)X_s + ZZ_s), \tag{3.8}$$

$$\frac{\partial p_0}{\partial n} = 0, \tag{3.9}$$

$$-\cos\phi(X_sZ_{ss} - X_{ss}Z_s)u_0^2 = -\frac{\partial p_1}{\partial n} - \frac{2u_0\cos\phi}{Rb} + \frac{\cos\phi}{Rb^2}((X+1)Z_s - ZX_s), \tag{3.10}$$

$$\frac{\partial p_0}{\partial \phi} = 0, \tag{3.11}$$

$$\sin\phi(X_sZ_{ss} - X_{ss}Z_s)u_0^2 = -\frac{1}{n}\frac{\partial p_1}{\partial \phi} + \frac{2u_0\sin\phi}{Rb} + \frac{\sin\phi}{Rb^2}(ZX_s - (X+1)Z_s), \tag{3.12}$$

$$u_0\frac{\mathrm{d}R_0}{\mathrm{d}s} = v_1 \quad \text{on } n = R_0, \tag{3.13}$$

$$p_0 = \frac{1}{R_0\,We} \quad \text{on } n = R_0, \tag{3.14}$$

$$p_1 = \frac{1}{We}\left(-\frac{1}{R_0^2}\left(R_1 + \frac{\partial^2 R_1}{\partial \phi^2}\right) + \cos\phi(X_sZ_{ss} - X_{ss}Z_s)\right) \quad \text{on } n = R_0, \tag{3.15}$$

$$v_1 = 0 \quad \text{on } n = 0 \tag{3.16}$$

$$X_s^2 + Z_s^2 = 1, \tag{3.17}$$

with $X_s = 1$, $X = Z = Z_s = 0$, $u_0 = R_0 = 1$ at $s = 0$. These equations, which represent a balance between pressure gradient, inertia and body force, can be integrated and simplified to give

$$p_0 = \frac{1}{R_0We}, \tag{3.18}$$

$$u_0 = \left(1 + \frac{1}{Rb^2}(X^2 + 2X + Z^2) + \frac{2}{We}\left(1 - \frac{1}{R_0}\right)\right)^{1/2}, \tag{3.19}$$

$$p_1 = \frac{n}{WeR_0}\cos\phi(X_sZ_{ss} - X_{ss}Z_s) + h_1(s), \tag{3.20}$$

$$v_1 = -\frac{n}{2}\frac{\mathrm{d}u_0}{\mathrm{d}s}, \tag{3.21}$$

$$Z_{ss} = \frac{WeR_0X_s}{WeR_0u_0^2 - 1}\left(\frac{2u_0}{Rb} + \frac{ZX_s - (X+1)Z_s}{Rb^2}\right), \tag{3.22}$$

$$R_{0,s} = -\frac{WeR_0^2((X+1)X_s + ZZ_s)}{Rb^2(2WeR_0u_0^2 + 1)}, \tag{3.23}$$

$$1 = X_s^2 + Z_s^2. \tag{3.24}$$

Also, $R_1 = h_2(s)\cos\phi + h_3(s)\sin\phi - h_1(s)WeR_0^2$ since R_1 is periodic with period 2π, where the $h_i(s)$ could be found at next order. However as we require only the leading-order equations to determine the centreline of the jet, this will not be done here.

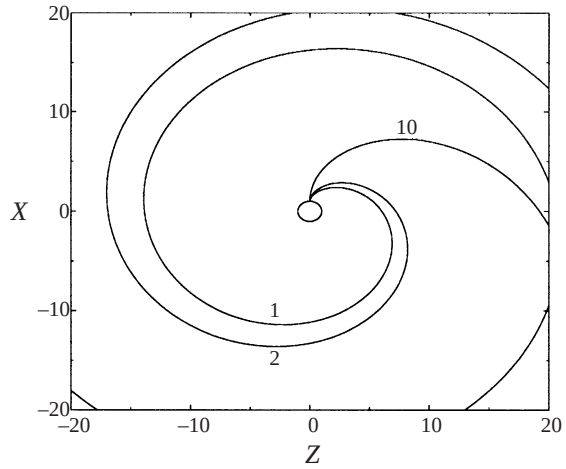

FIGURE 5. The effects of variations in rotation on the centreline of a jet in the (X, Z)-plane for various values of the Rossby number $Rb = 1, 2, 10$, with no surface tension ($We = \infty$). Here the origin has been translated to the centre of the container.

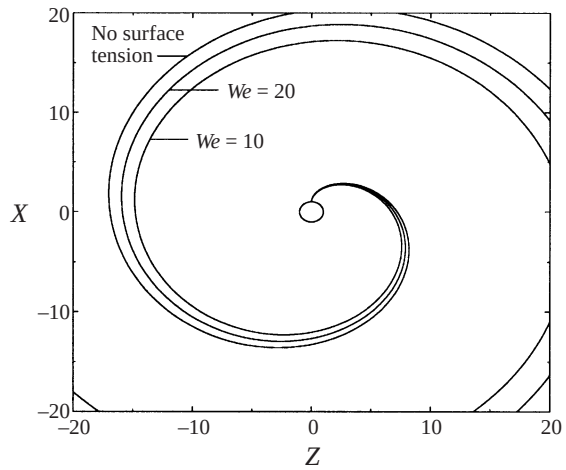

FIGURE 6. The centreline of a jet in the (X, Z)-plane for various Weber numbers ($We = 10, 20, \infty$) with $Rb = 2$ (note $We = \infty$ corresponds to no surface tension). The loops with a smaller value of the Weber number are more tightly coiled. Here the origin has been translated to the centre of the container.

Equations (3.22), (3.23) and (3.24) are a set of nonlinear ordinary differential equations for X, Z and R_0. This system of equations is solved numerically using a FORTRAN 77 program calling a NAG routine (D02BBF) that uses a Runge–Kutta–Merson method subject to the initial conditions $X_s = 1$, $X = Z = Z_s = 0$, $R_0 = u_0 = 1$.

Figures 5 and 6 show the centreline of the steady jet for various parameter values. The small circle at the origin represents the container. The graphs in figure 5 show the trajectory for various values of the Rossby number for fixed (infinite) Weber number. Smaller Rossby numbers correspond to more tightly coiled loops. On figure 6 the graphs show the centreline for zero surface tension $We = \infty$, $We = 20$ and $We = 10$ for $Rb = 2$. The loops with a smaller value of the Weber number are more tightly

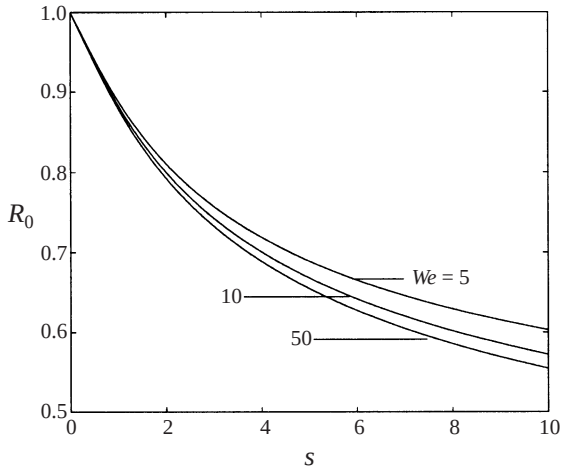

FIGURE 7. The behaviour of arclength s against the radius of the jet for various Weber numbers ($Rb = 2$).

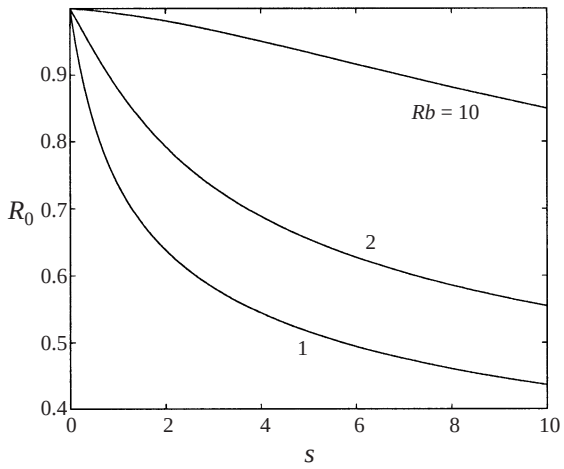

FIGURE 8. The behaviour of arclength s against the radius of the jet for various Rossby numbers ($We = 50$).

coiled. Figures 7 and 8 show how the radius of the jet R_0 varies with arclength s for various Weber and Rossby numbers. The graphs show that the jet thins as it leaves the orifice, as expected.

We find that there is a singularity at $We = 1$. This agrees with a number of papers on liquid jets and sheets (see introduction). For $0 < We \leqslant 1$ we obtain no sensible solutions. In this case the liquid emerges from the orifice too slowly to form a coherent jet.

The numerics reveal that for $1 < We < \infty$ there exists a constant $s^* > 0$ such that at $s = s^*$, u_0 reaches a maximum and R_0 reaches a minimum. For an example of this situation see figure 9. Figure 10 shows that the value of s^* increases rapidly as the Weber number is increased. We note that $s^* \to \infty$ as $We \to \infty$. For moderately large values of the Weber number s^* is very large. This explains why the minimum is not shown on figures 7 and 8. When $s \gg s^*$, R_0 becomes large and the slender jet assumption breaks down, and hence the asymptotic procedure is no longer valid

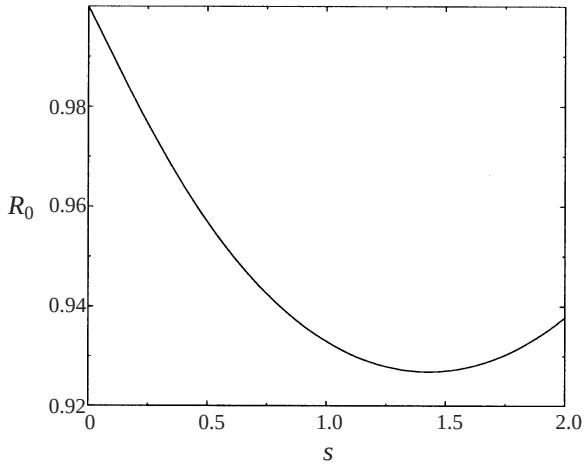

FIGURE 9. Arclength s against the radius of the jet for $We = 1.5$ and $Rb = 2$.

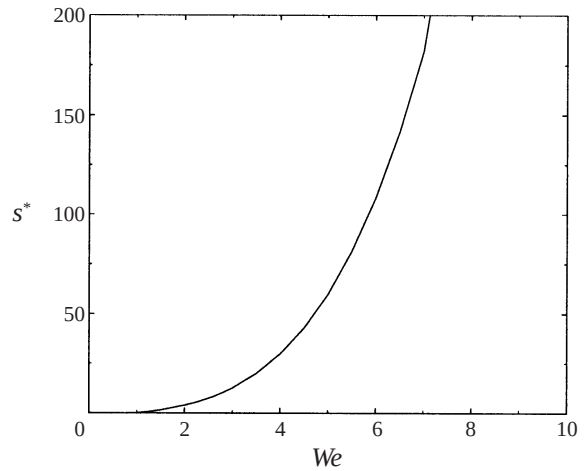

FIGURE 10. Graph showing the value of s^* against Weber number ($Rb = 2$).

as $s \to \infty$ for finite Weber number. However, since s^* is very large for even modest values of the Weber number, the jet will almost certainly have broken up before it reaches $s = s^*$ (in the prilling process the jet is always observed to break up when $s = O(1)$), and therefore this phenomenon is only of concern for fairly small values of $We - 1$.

When $We - 1$ is fairly small we have an exceptional case (see Keller & Weitz 1957). Here the value of s^* is $\leqslant O(1)$ and the jet could possibly reach $s = s^*$ before breakup. This suggests that something different happens as the Weber number tends to one, and the slender jet theory may no longer apply. This exceptional case will be looked at in future work. As an example, if we consider water, taking $We = 1.1$, $\rho = 1000\,\mathrm{kg\,m^{-3}}$, $\sigma = 0.07\,\mathrm{kg\,s^{-2}}$, we find that $U^2 a = 0.00008\,\mathrm{m^3\,s^{-2}}$, which corresponds to a slow or a thin jet.

4. Temporal stability of steady-state solutions

A linear stability analysis of our steady solutions is now performed. The lengthscale over which the centreline curves is $s = O(1)$, but we know that the radius of the droplets caused by jet instability is of order a, which is comparable with ϵ when $s = O(1)$. We consider travelling wave modes of the form $\exp(\mathrm{i}k\bar{s} + \lambda\bar{t})$, where $\bar{s} = s/\epsilon$, $\bar{t} = t/\epsilon$, $k = k(s) = O(1)$ and $\lambda = \lambda(s) = O(1)$, so that we have a multiple scales formulation giving rise to perturbations with wavelength of $O(\epsilon)$, as required. Note that for the travelling wave to propagate away from the orifice, we require $\mathrm{Re}(k)\mathrm{Im}(\lambda) < 0$. We perturb the steady solutions found in the previous subsection in the following way:

$$\left.\begin{aligned} \boldsymbol{u} &= \boldsymbol{u}(s,n,\phi,\epsilon) + \delta\tilde{\boldsymbol{u}}(s,\bar{s},n,\phi,t,\bar{t}\,),\\ R &= R(s,\phi,\epsilon) + \delta\tilde{R}(s,\bar{s},\phi,t,\bar{t}\,),\\ p &= p(s,n,\phi,\epsilon) + \delta\tilde{p}(s,\bar{s},n,\phi,t,\bar{t}\,),\\ \boldsymbol{X} &= \boldsymbol{X}(s,\epsilon) + \delta\epsilon\tilde{\boldsymbol{X}}(s,\bar{s},t,\bar{t}\,), \end{aligned}\right\} \tag{4.1}$$

where $\tilde{\boldsymbol{u}} = \tilde{u}\boldsymbol{e}_s + \tilde{v}\boldsymbol{e}_n + \tilde{w}\boldsymbol{e}_\phi$, $\boldsymbol{X} = X\boldsymbol{i} + Z\boldsymbol{k}$, $\tilde{\boldsymbol{X}} = \tilde{X}\boldsymbol{i} + \tilde{Z}\boldsymbol{k}$ and δ is a small dimensionless parameter. (We note that we first tried $\hat{\boldsymbol{X}} = \tilde{\boldsymbol{X}}_0(s,\bar{s},t,\bar{t}\,) + \epsilon\tilde{\boldsymbol{X}}(s,\bar{s},t,\bar{t}\,)$, but $\tilde{\boldsymbol{X}}_0$ was found to be identically equal to zero.) We substitute (4.1) into the jet equations given in § 2, retaining linear terms in δ only. We then substitute into these equations the asymptotic series in ϵ obtained in § 3 for the steady state. At order δ we obtain

$$n\frac{\partial\tilde{u}}{\partial\bar{s}} + \tilde{v} + n\frac{\partial\tilde{v}}{\partial n} + \frac{\partial\tilde{w}}{\partial\phi} = 0, \tag{4.2}$$

$$\frac{\partial\tilde{u}}{\partial\bar{t}} + u_0(s)\frac{\partial\tilde{u}}{\partial\bar{s}} = -\frac{\partial\tilde{p}}{\partial\bar{s}}, \tag{4.3}$$

$$\frac{\partial\tilde{v}}{\partial\bar{t}} + u_0(s)\frac{\partial\tilde{v}}{\partial\bar{s}} + u_0(s)\cos\phi\left(Z_s\frac{\partial^2\tilde{X}}{\partial\bar{s}\partial\bar{t}} - X_s\frac{\partial^2\tilde{Z}}{\partial\bar{s}\partial\bar{t}}\right) - \cos\phi\left(X_s\frac{\partial^2\tilde{Z}}{\partial\bar{s}^2} - Z_s\frac{\partial^2\tilde{X}}{\partial\bar{s}^2}\right)u_0^2(s) = -\frac{\partial\tilde{p}}{\partial n}, \tag{4.4}$$

$$\frac{\partial\tilde{w}}{\partial\bar{t}} + u_0(s)\frac{\partial\tilde{w}}{\partial\bar{s}} + u_0(s)\sin\phi\left(X_s\frac{\partial^2\tilde{Z}}{\partial\bar{s}\partial\bar{t}} - Z_s\frac{\partial^2\tilde{X}}{\partial\bar{s}\partial\bar{t}}\right) + \sin\phi\left(X_s\frac{\partial^2\tilde{Z}}{\partial\bar{s}^2} - Z_s\frac{\partial^2\tilde{X}}{\partial\bar{s}^2}\right)u_0^2(s) = -\frac{1}{n}\frac{\partial\tilde{p}}{\partial\phi}, \tag{4.5}$$

$$\frac{\partial\tilde{R}}{\partial\bar{t}} + \left(Z_s\frac{\partial\tilde{X}}{\partial\bar{t}} - X_s\frac{\partial\tilde{Z}}{\partial\bar{t}}\right)\cos\phi - \tilde{v} + u_0(s)\frac{\partial\tilde{R}}{\partial\bar{s}} = 0 \quad \text{on } n = R_0, \tag{4.6}$$

$$\tilde{p} = \frac{1}{We}\left(-\frac{1}{R_0^2}\left(\tilde{R} + \frac{\partial^2\tilde{R}}{\partial\phi^2}\right) + \cos\phi\left(X_s\frac{\partial^2\tilde{Z}}{\partial\bar{s}^2} - Z_s\frac{\partial^2\tilde{X}}{\partial\bar{s}^2}\right) - \frac{\partial^2\tilde{R}}{\partial\bar{s}^2}\right) \quad \text{on } n = R_0, \tag{4.7}$$

$$\tilde{v} = \tilde{w} = 0 \quad \text{on } n = 0, \tag{4.8}$$

$$X_s\frac{\partial\tilde{X}}{\partial\bar{s}} + Z_s\frac{\partial\tilde{Z}}{\partial\bar{s}} = 0. \tag{4.9}$$

We will now look for the most general solutions to our stability problem above by posing the following series solutions for the disturbance travelling wave modes:

$$\tilde{u} = \mathrm{i}(\exp(\mathrm{i}k(s)\bar{s} + \lambda(s)\bar{t}\,)) \left(\bar{u}_1(n,s) + \sum_{m=1}^{\infty} \bar{u}_{m0}(n,s)\cos(m\phi) + \bar{u}_{m1}(n,s)\sin(m\phi) \right) + \text{c.c.}, \tag{4.10}$$

$$\tilde{v} = (\exp(\mathrm{i}k(s)\bar{s} + \lambda(s)\bar{t}\,)) \left(\bar{v}_1(n,s) + \sum_{m=1}^{\infty} \bar{v}_{m0}(n,s)\cos(m\phi) + \bar{v}_{m1}(n,s)\sin(m\phi) \right) + \text{c.c.}, \tag{4.11}$$

$$\tilde{w} = (\exp(\mathrm{i}k(s)\bar{s} + \lambda(s)\bar{t}\,)) \left(\bar{w}_1(n,s) + \sum_{m=1}^{\infty} \bar{w}_{m0}(n,s)\cos(m\phi) + \bar{w}_{m1}(n,s)\sin(m\phi) \right) + \text{c.c.}, \tag{4.12}$$

$$\tilde{p} = (\exp(\mathrm{i}k(s)\bar{s} + \lambda(s)\bar{t}\,)) \left(\bar{p}_1(n,s) + \sum_{m=1}^{\infty} \bar{p}_{m0}(n,s)\cos(m\phi) + \bar{p}_{m1}(n,s)\sin(m\phi) \right) + \text{c.c.}, \tag{4.13}$$

$$\tilde{R} = (\exp(\mathrm{i}k(s)\bar{s} + \lambda(s)\bar{t}\,)) \left(\bar{R}_1(s) + \sum_{m=1}^{\infty} \bar{R}_{m0}(s)\cos(m\phi) + \bar{R}_{m1}(s)\sin(m\phi) \right) + \text{c.c.}, \tag{4.14}$$

$$\tilde{X} = \exp(\mathrm{i}k(s)\bar{s} + \lambda(s)\bar{t}\,)\bar{X}_1 + \text{c.c.}, \tag{4.15}$$

$$\tilde{Z} = \exp(\mathrm{i}k(s)\bar{s} + \lambda(s)\bar{t}\,)\bar{Z}_1 + \text{c.c.}, \tag{4.16}$$

where c.c. denotes complex conjugate.

Substituting these series into (4.2)–(4.9) we obtain

$$\left.\begin{aligned} \bar{u}_1 = AI_0(kn), \quad \bar{v}_1 = AI_1(kn), \\ \bar{w}_1 = 0, \quad \bar{p}_1 = -\frac{A(\lambda + \mathrm{i}ku_0)I_0(kn)}{k}, \end{aligned}\right\} \tag{4.17}$$

$$\left.\begin{aligned} \bar{u}_{10} = BI_1(kn), \quad \bar{v}_{10} = B\left(I_0(kn) - \frac{I_1(kn)}{kn}\right) - \frac{\mathrm{i}ku_0\bar{X}_1}{Z_s}, \\ \bar{w}_{11} = \frac{\mathrm{i}ku_0\bar{X}_1}{Z_s} - \frac{BI_1(kn)}{kn}, \quad \bar{p}_{10} = -\frac{B(\lambda + \mathrm{i}ku_0)I_1(kn)}{k}, \\ \bar{Z}_1 = -\frac{X_s\bar{X}_1}{Z_s}, \end{aligned}\right\} \tag{4.18}$$

$$\left.\begin{aligned} \bar{u}_{m0} = C_mI_m(kn), \quad \bar{v}_{m0} = \frac{C_m}{k}\frac{d}{dn}(I_m(kn)), \\ \bar{w}_{m1} = -\frac{mC_mI_m(kn)}{kn}, \quad \bar{p}_{m0} = -\frac{C_m(\lambda + \mathrm{i}ku_0)I_m(kn)}{k} \quad \text{for } m > 1, \end{aligned}\right\} \tag{4.19}$$

$$\left.\begin{aligned} \bar{u}_{m1} = D_mI_m(kn), \quad \bar{v}_{m1} = \frac{D_m}{k}\frac{d}{dn}(I_m(kn)), \\ \bar{w}_{m0} = \frac{mD_mI_m(kn)}{kn}, \quad \bar{p}_{m1} = -\frac{D_m(\lambda + \mathrm{i}ku_0)I_m(kn)}{k} \quad \text{for } m \geqslant 1, \end{aligned}\right\} \tag{4.20}$$

$$\left.\begin{aligned} \bar{R}_1 = \frac{\bar{v}_1}{\lambda + \mathrm{i}ku_0}, \quad \bar{R}_{10} = \frac{Z_s\bar{v}_{10} - \lambda\bar{X}_1}{Z_s(\lambda + \mathrm{i}ku_0)}, \quad \bar{R}_{m0} = \frac{\bar{v}_{m0}}{\lambda + \mathrm{i}ku_0} \quad \text{for } m \geqslant 1, \\ \bar{R}_{m1} = \frac{\bar{v}_{m1}}{\lambda + \mathrm{i}ku_0} \quad \text{for } m \geqslant 1 \quad \text{on } n = R_0, \end{aligned}\right\} \tag{4.21}$$

$$\left.\begin{aligned} \bar{p}_1 = \frac{\bar{R}_1}{We}\left(k^2 - \frac{1}{R_0^2}\right), \quad \bar{p}_{10} = \frac{1}{We}\left(\frac{k^2\bar{X}_1}{Z_s} + k^2\bar{R}_{10}\right), \\ \bar{p}_{m0} = \frac{\bar{R}_{m0}}{We}\left(-\frac{1}{R_0^2}(1-m^2) + k^2\right) \quad \text{for } m > 1, \\ \bar{p}_{m1} = \frac{\bar{R}_{m1}}{We}\left(-\frac{1}{R_0^2}(1-m^2) + k^2\right) \quad \text{for } m \geqslant 1 \quad \text{on } n = R_0, \end{aligned}\right\} \tag{4.22}$$

where A, C, D and $\bar{X}_1$ are arbitrary functions of s, $B = 2\mathrm{i}ku_0\bar{X}_1/Z_s$, I_0, I_1 and I_m are the zeroth-, first- and mth-order modified Bessel functions, respectively, and m is an integer. We note that equations (4.17), (4.18), (4.19) and (4.20) will each give rise to a different eigenvalue λ.

If we now substitute the solutions into these boundary conditions we obtain the eigenvalue relation

$$(\lambda_m + \mathrm{i}ku_0)^2 = \frac{1}{We}\left(\frac{1}{R_0^2}(1-m^2) - k^2\right)k\frac{I_m'(kR_0)}{I_m(kR_0)}, \tag{4.23}$$

where m represents the parameter associated with the azimuthal terms in the Fourier expansion and $I_m'(kR_0)$ represents $(\mathrm{d}/\mathrm{d}x\, I_m(x))|_{x=kR_0}$. Also, we have written $\lambda = \lambda_m$ to distinguish between each mode.

We will now interpret equation (4.23) in terms of temporal stability. We consider an instability mode of the form $\exp(\mathrm{i}k\bar{s} + \lambda\bar{t})$ where λ is complex and k is real. For an unstable mode we require $\mathrm{Re}(\lambda) > 0$. From equation (4.23) we obtain an infinite number of neutrally stable eigenvalues (which corresponds to λ_m being purely imaginary) for the problem and one unstable eigenvalue. The neutrally stable eigenvalues are given by

$$\lambda_m = -\mathrm{i}ku_0 \pm \sqrt{\frac{1}{We}\left(\frac{1}{R_0^2}(1-m^2) - k^2\right)k\frac{I_m'(kR_0)}{I_m(kR_0)}}, \tag{4.24}$$

for $m \neq 0$. On first inspection this mode looks similar to the classic Rayleigh mode (given by equation (1.1)). However, this mode varies with the arclength along the jet.

The unstable mode (corresponding to the ϕ independent part of (4.10)–(4.14)) is given by

$$\lambda_0 = -\mathrm{i}ku_0 \pm \sqrt{\frac{1}{We}\left(\frac{1}{R_0^2} - k^2\right)k\frac{I_1(kR_0)}{I_0(kR_0)}}. \tag{4.25}$$

The mode given by (4.25) is unstable when $0 < k < 1/R_0$, since $\mathrm{Re}(\lambda_0) > 0$. We find that the most unstable mode occurs when $k = k^* = 0.697/R_0$. Therefore the most unstable mode has a wavenumber which varies with s.

We now show graphically how the growth rate and corresponding wavenumber for this most unstable mode varies with arclength s for various Rossby and Weber numbers. Figures 11(a) and 12(a) show the growth rate $\mathrm{Re}(\lambda_0)$ for the most unstable mode plotted against arclength. Figures 11(b) and 12(b) show the wavenumber which corresponds to the most unstable mode k^* against s.

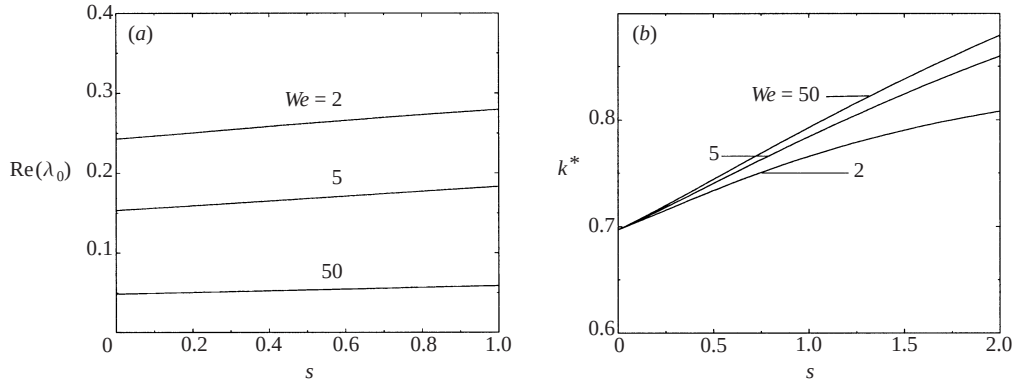

FIGURE 11. Arclength s against (a) the growth rate $\mathrm{Re}(\lambda_0)$ of the most unstable mode and (b) k^* for various Weber numbers ($Rb = 2$).

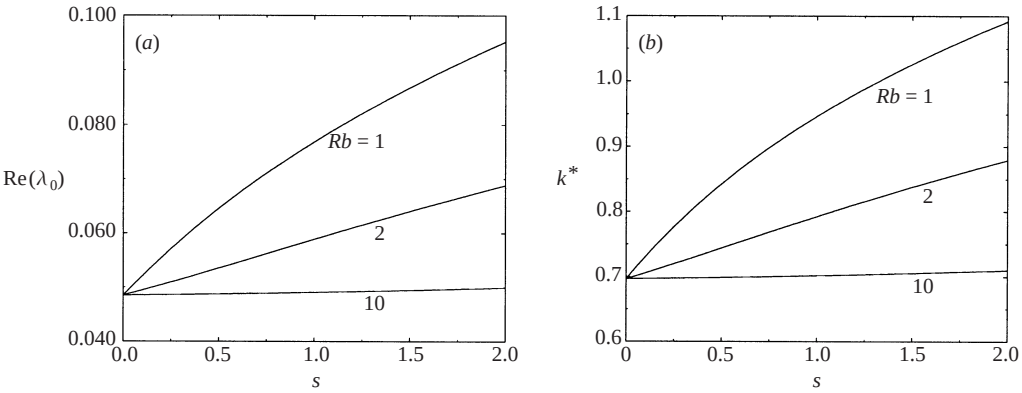

FIGURE 12. Arclength s against the (a) growth rate $\mathrm{Re}(\lambda_0)$ of the most unstable mode and (b) k^* for various Rossby numbers ($We = 50$).

The functions A, B, C, D, $\bar{X}_1$ and $\bar{Z}_1$ are not determined here. When these functions appear in the above equations they can be eliminated. For example when A appears it cancels throughout. Therefore in a linear theory the precise determination of these is not necessary. If we performed a weakly nonlinear analysis then they would be found at higher-order using secularity conditions. The secularity condition would be found at order δ^3 where a Landau type equation would be obtained.† This weakly nonlinear calculation would only give a small correction to the prediction of linear theory. Since the breakup mechanism is strongly nonlinear a weakly nonlinear theory would give little extra information.

5. Spatial stability of steady-state solutions

We also consider spatial as well as temporal stability, following Keller *et al.* (1973). We again consider an instability mode of the form $\exp(\mathrm{i}k(s)\bar{s} + \lambda(s)\bar{t})$ where k is considered complex while λ ($= -\mathrm{i}\omega$) is purely imaginary (where ω is the real frequency). The mode is unstable when $\mathrm{Im}(k) < 0$, and the largest growth rate will correspond to the most negative value of $\mathrm{Im}(k)$. As we are considering the same mode

† We expect the perturbations to satisfy $\delta^2 = \epsilon$, as in Schulkes (1993). Though the linear stability analysis will still be valid even if this distinguished limit does not apply here.

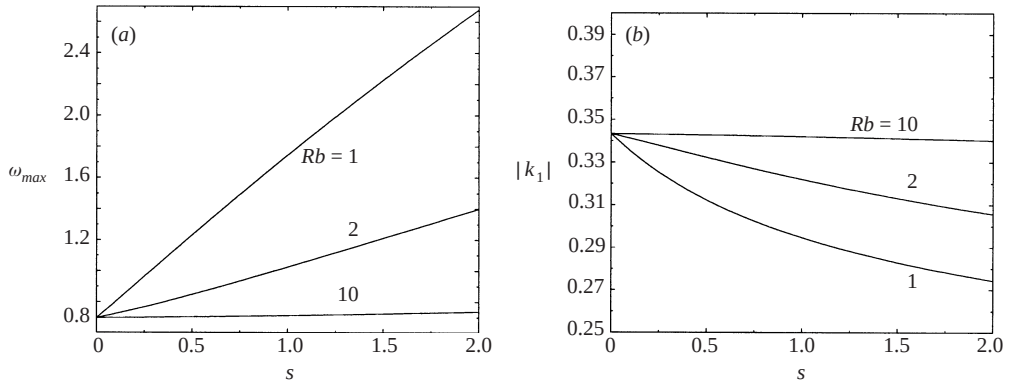

FIGURE 13. Arclength s against (a) the frequency which corresponds to the most unstable mode and (b) the modulus of the growth rate $|k_1|$ of the most unstable mode for various Rossby numbers ($We = 50$).

we obtain the same eigenvalue relation for the problem, namely

$$WeR_0^2 I_m(kR_0)(\omega - ku_0)^2 = kI_m'(kR_0)(R_0^2k^2 + (m^2 - 1)). \tag{5.1}$$

Prior to a numerical solution of this it is worthwhile constructing the large Weber number asymptotics of (5.1), looking for solutions of k in the following series:

$$k = k_0 + k_1 We^{-1/2} + k_2 We^{-1} + \cdots, \tag{5.2}$$

as $We \to \infty$.

Substituting this series for k into (5.1) we obtain two solutions given by

$$k_0 = \frac{\omega}{u_0}, k_1 = \pm \left(\frac{\omega I_m'(\omega R_0/u_0)(\omega^2 R_0^2 + u_0^2(m^2 - 1))}{R_0^2 u_0^5 I_m(\omega R_0/u_0)} \right)^{1/2}, \tag{5.3}$$

$$k_0 = \pm \frac{ij_{mn}}{R_0}, \quad k_1 = 0, \quad k_2 = \frac{(2\omega R_0 j_{mn} u_0 \mp \mathrm{i}(\omega^2 R_0^2 - j_{mn}^2 u_0^2))j_{mn}(j_{mn}^2 - m^2 + 1)}{(\omega^2 R_0^2 + j_{mn}^2 u_0^2)^2}, \tag{5.4}$$

where j_{mn} is the nth positive root of the Bessel function J_m.

From (5.3) we see that k_0 is real. The correction k_1 is real when $m \neq 0$. When $m = 0$, k_1 is real for $\omega^2 R_0^2 \geqslant u_0^2$. These all correspond to neutrally stable spatial modes. The correction k_1 is complex when $m = 0$ and $\omega^2 R_0^2 < u_0^2$. This complex case represents a spatially unstable travelling wave mode when the negative alternative sign in (5.3) is chosen. (The positive alternative sign in (5.3) represents a spatially stable solution.) This spatially unstable solution has $O(1)$ wavelength, $O(1)$ phase speed and $O(We^{-1/2})$ growth rate.

From (5.4) we see that k_0 is purely imaginary, while k_2 is complex. The negative alternative sign in k_0 in (5.4) corresponds to spatially unstable modes (and the positive sign represents spatially stable modes). The growth rate of these spatially unstable modes are $O(1)$ but the wavelengths are $O(We)$, so that these are long-wavelength modes. The main droplets produced by breakup will have a diameter which is comparable to the diameter of the jet. These droplets will be produced by an unstable mode for which the real part of k is $O(1)$. Consequently, we do not expect the unstable modes given by (5.4) to be as important physically as those given by (5.3).

Figures 13(a) and 13(b) show the most unstable mode associated with (5.3) for the large Weber number asymptotics. Figure 13(a) shows the frequency of the most

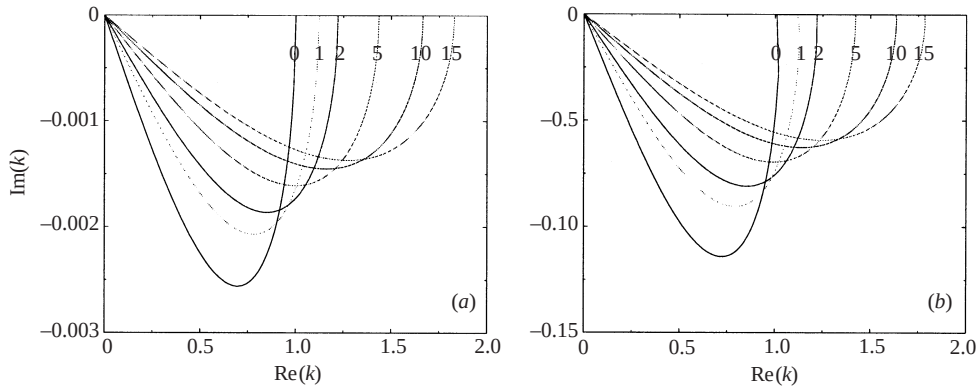

FIGURE 14. Graph showing numerically Re(k) against Im(k) for various values of s $Rb = 2$: (a) $We = 50$, (b) $We = 10$. The frequency ω is real on each line, but varies from 0 to ∞ along each line from left to right.

unstable mode given by (5.3) against s for various Rossby numbers. Figure 13(b) shows the growth rate of the most unstable mode given by (5.3).

Figures 14(a) and 14(b) show numerical solutions to (5.1). On each line ω is real. The most unstable mode for each value of s occurs at the minimum point on each curve. The $|\mathrm{Im}(k)|$ decreases as arclength s increases. However, this still produces a growth rate which increases with s since the actual growth rate is equal to $-\bar{s}\mathrm{Im}(k) = -s\mathrm{Im}(k)/\epsilon$. The numerical results from figure 14(a) agree with our large Weber number asymptotics. It can be seen that the modes are spatially unstable, in each case.

6. Experiments

We will now describe a series of experiments to verify the trends that the theory predicts, performed in the Applied Mathematics Laboratory at the University of Birmingham.

The apparatus consists of a cylindrical can (diameter = 8.5 cm, height = 11.5 cm) that contains two small holes (diameters of 1 mm or 3 mm respectively at opposite ends of a diameter). This can is attached by means of a long thin paddle to an electronic stirrer (Heidolph Stirrer – Model RZR2021) with digitally controlled rotation rate (in a clockwise direction). A tube is fed into the can from a tap to allow a continuous water supply. This apparatus is all contained in a transparent tank that collects the excess water. The trajectory of the jet is captured by means of a high-speed digital camera (Kodak MotionCorder 3000, with a capture rate of up to 3000 frames per second). The images from the camera were loaded into Image-Pro Express from which we can take digital measurements accurate to a tenth of a millimetre.

In the paper so far we have worked in a rotating frame of reference. All the theoretical results that we have produced have been in this rotating frame. As the experimental pictures that we will produce are not in a rotating frame we will need to convert back to the non-rotating frame when we compare the theory to the experiments. For the various different experiments we need to calculate the exit speed of a jet as it leaves the hole. The exit speed of the jet in the non-rotating frame is calculated using the formula

$$U_1 = \sqrt{(s_0\Omega)^2 + U^2}, \tag{6.1}$$

where U is the speed in the rotating frame.

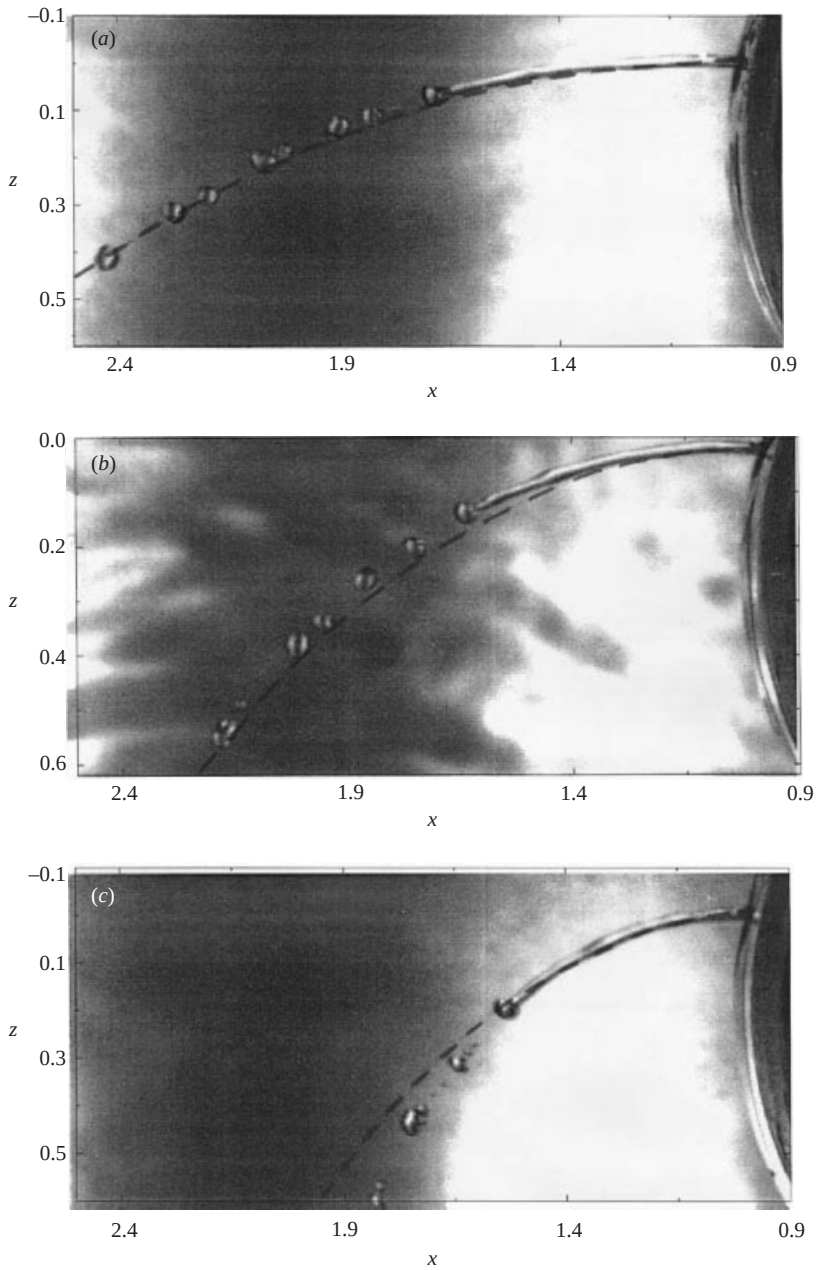

FIGURE 15. Pictures of a jet emerging from the small hole with the can rotating, showing experiments against theory (dashed line) for different rotation rates: (*a*) 50 r.p.m., (*b*) 100 r.p.m., (*c*) 200 r.p.m. Note that the Weber number is not constant in the above three pictures.

Figure 15(*a–c*) shows three different jets emanating from the smaller hole. The dotted lines on the figures correspond to the centreline of the jets predicted by the theory in each case. Figure 15(*a*) shows a picture of a jet that is leaving the can, rotating at 50 r.p.m. It can be seen clearly that the jet breaks up into a number of droplets. These droplets are of slightly different sizes. This may be due to a slight

Rotation rate (r.p.m.)	Exit speed U_1 ($m\,s^{-1}$)	Breakup length divided by initial jet radius
62	1.16	20.5
101	1.22	21.3
155	1.32	22.0
167	1.35	22.5
51	1.54	22.5
58	1.54	22.0
100	1.58	22.1
105	1.59	24.9
147	1.65	30.0
179	1.72	31.3

TABLE 1. Table of breakup lengths for experiments using the 3 mm hole.

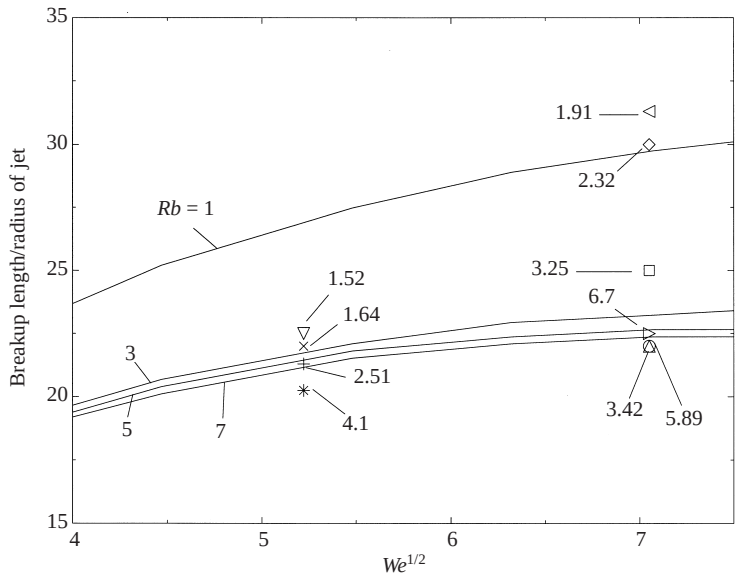

FIGURE 16. Theoretical predictions of $We^{1/2}$ against the breakup length of the jet divided by the jet radius (at the orifice) produced from linear spatial stability for various Rossby numbers. The symbols correspond to the experimental data points obtained from the 3 mm hole in the experiment. The Rossby number of each theoretical curve and each data point is indicated. The Weber number was varied in the experiment by varying the ambient water level in the container. In this graph, $|A| = 0.24$. This single value for $|A|$ was found by fitting theory to experimental data. Here $\epsilon = 0.0353$.

instability that occurs in the form of the can vibrating when it is rotated (although for a straight jet droplets are also of different sizes). The droplets that are observed are approximately the same size as the radius of the hole.

Figure 15(*b*) shows a picture of a jet that is leaving the can rotating at 100 r.p.m. From this picture it can be seen that the jet is more curved than at 50 r.p.m. for this higher rotation rate. This agrees with our theory.

Figure 15(*c*) shows a jet that leaves the can when it is rotating at a speed of 200 r.p.m. (though for a lower *We* than in the previous two pictures). We can also see that this jet is even more curved than in the previous two cases due to the higher rotation rate. The formation of satellite droplets can be clearly seen. These are not

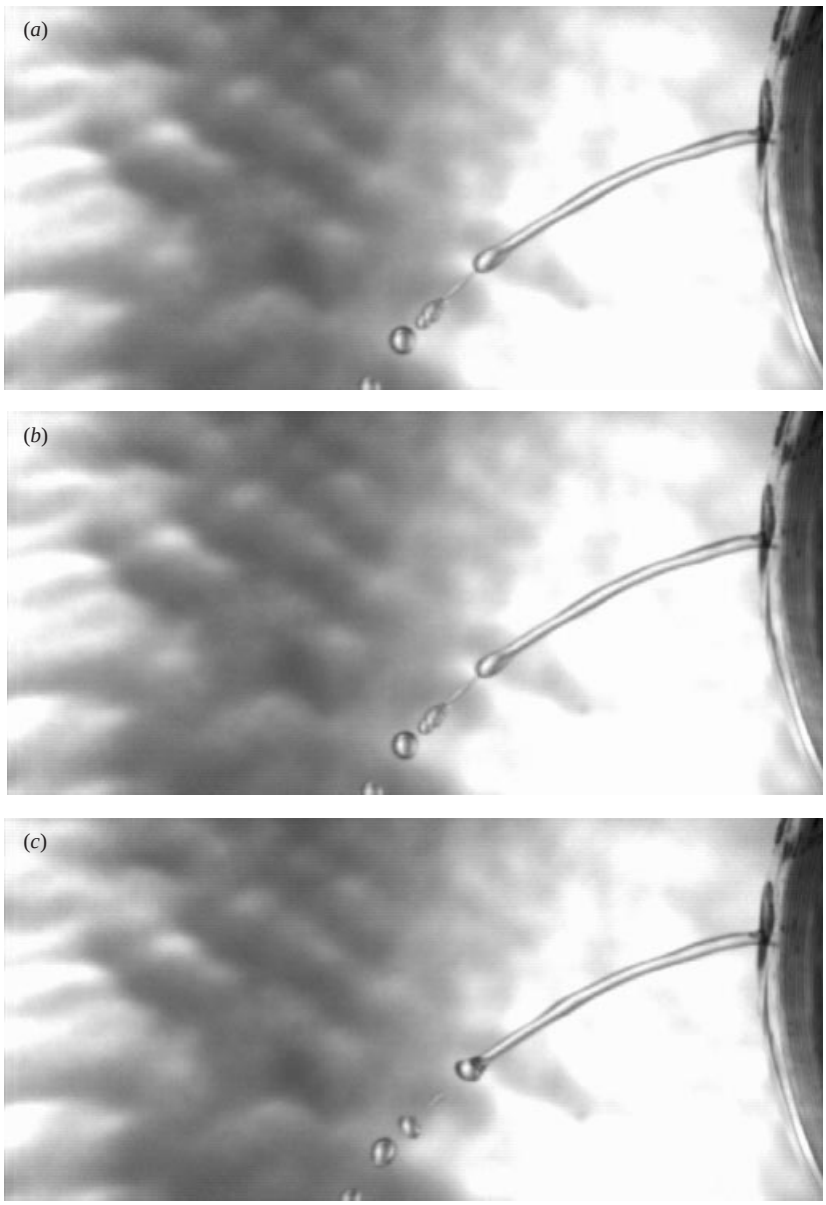

FIGURE 17 (*a–c*). For caption see facing page.

predicted by the linear theory as they are a nonlinear effect. From figure 15(*a–c*) we can see that the theoretical trajectories for the jets' centrelines are in reasonably good agreement with the experiments. The deviation between the two may be due to the fact that air resistance has not been taken into account in the model.

To estimate the breakup length from the linear stability results we require

$$\left| \epsilon^{1/2} A \frac{I_1(kR_0)}{\lambda + \mathrm{i}ku_0} \exp(-k_i s/\epsilon) \right| = R_0(s), \tag{6.2}$$

as in Middleman (1995). Measured breakup lengths are shown in table 1 for the

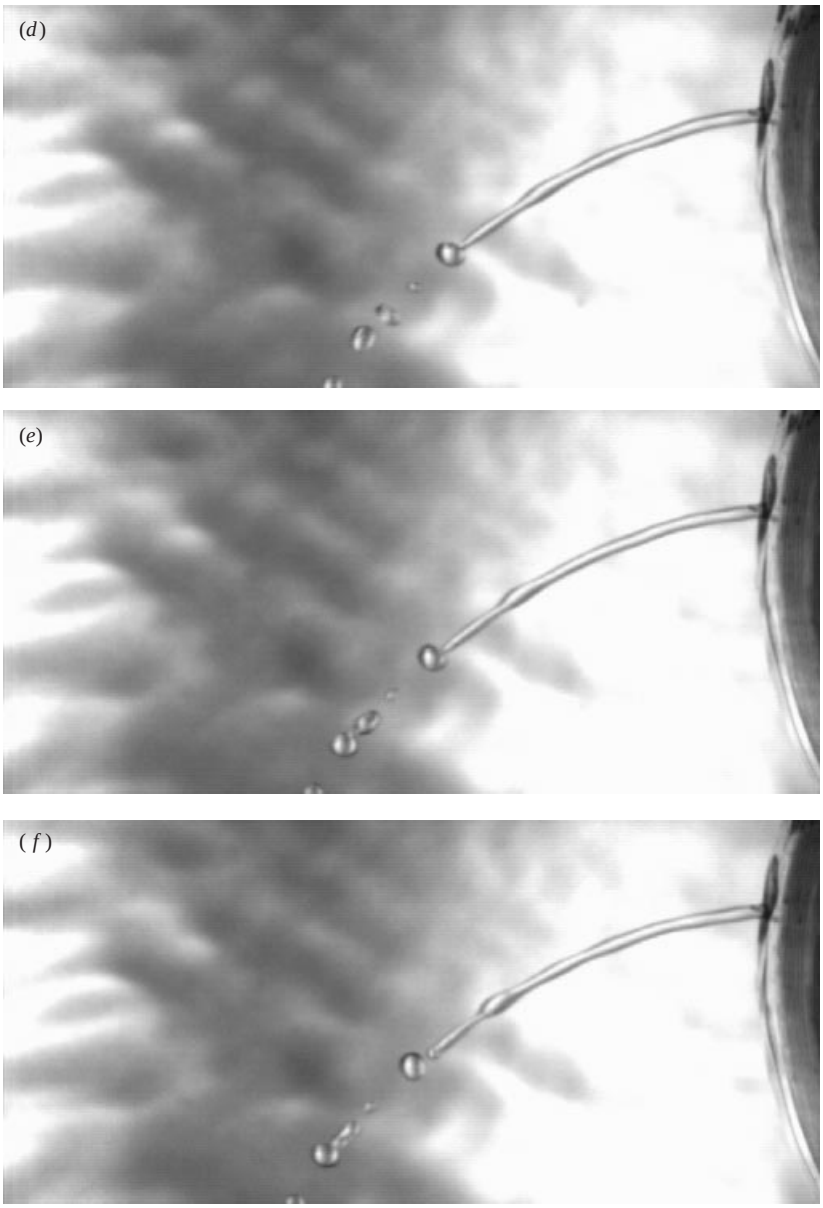

FIGURE 17. Pictures of a jet emerging from the small hole with the can rotating at a rate of 100 r.p.m., showing progressive time steps: (*a*) $t = 0.0130$ s, (*b*) 0.0135 s, (*c*) 0.0140 s, (*d*) 0.0145 s, (*e*) 0.0150 s, (*f*) 0.0155 s.

larger of the two holes. This shows a general trend for the breakup length divided by the initial jet radius to increase with U_1. Figure 16 shows the theoretical predictions against experimental data for the breakup length of the jet emerging from this hole. The experimental data are in reasonable agreement with the theory. We have fitted the theoretical lines to the data points on the graph (as in Middleman 1995). In order to do this, for figure 16, $|A| = 0.24$. Figure 16 suggests that the jet breaks up further away from the orifice for lower Rossby number. Also, increasing the Weber number increases the breakup length, as with straight jets. There are discrepancies between the

data points and the theory. This may be because we have used a linear theory, while the breakup mechanism is a nonlinear effect. Also, it is difficult to achieve $s_0\Omega^2 \gg g$ in our experiments (due to the small scale) so the jets produced do not exactly lie in a plane.

We will now show in more detail the dynamics of jet breakup. Figure 17(*a–f*) shows the breakup of a liquid jet that is leaving the smaller hole in our rotating can. The figures show progressive time steps with a time between each picture of 0.0005 s. In figure 17(*a*) we can see that a droplet is starting to be formed at the end of the jet. The detachment of this droplet from the jet can then be seen in the next sequence of pictures. The droplet is completely detached by the time indicated in figure 17(*f*). Figure 17(*f*) also shows that as the droplet forms, a secondary droplet forms on the tip of the thread. On figure 17(*e*) we can see that just before the droplet separates it forms a conical connection with the thread (a similar phenomenon was noted by Peregrine, Shoker & Symon 1990). Figure 17(*d*,*f*) shows a swell in the liquid jet being amplified and propagating towards the nascent droplet at the end of the thread. This swell will form the next droplet in the sequence. The breakup is better shown by a movie, found at http://www.mat.bham.ac.uk/I.M.Wallwork.

7. Conclusions

The trajectory of a rotating, slender inviscid jet emanating from a small hole has been determined. We have considered the temporal stability of the steady flows of this jet using asymptotic methods, and found a mode which appears superficially similar to the classical Rayleigh mode. However our mode is a function of the long lengthscale s and varies slowly with arclength along the jet. We have extended the spatial stability work of Keller *et al.* (1973) to include our long lengthscale s. Finally we have performed a series of small-scale experiments looking at the trajectory and breakup of slender liquid jets, finding reasonably good agreement between theory and experiments.

The methods described here are applicable to other situations. For example the dynamics of a jet draining under gravitational body force (without rotation) and a full three-dimensional problem with both gravity and rotation can be solved using a similar method (see Wallwork, Decent & King 2000; Wallwork 2001).

I. M. Wallwork would like to thank *Norsk Hydro* and EPSRC for their financial support during this work.

REFERENCES

Andersen, K. G. & Yttri, G. 1997 *Et Porsϕk verdt*. Univesitets for laget Oslo.

Anno, J. N. 1977 *The Mechanics of Liquid Jets*. Lexington Books.

Baird, M. H. I. & Davidson, J. F. 1962 Annular jets-I Fluid dynamics. *Chem. Engng Sci.* **17**, 467–472.

Bogy, D. B. 1979 Drop formation in a circular liquid jet. *Annu. Rev. Fluid. Mech.* **11**, 207–228.

Chaudhary, K. C. & Maxworthy, T. 1980*a* The nonlinear capillary instability of a liquid jet. Part 2. Experiments on jet behaviour before droplet formation. *J. Fluid Mech.* **96**, 275–286.

Chaudhary, K. C. & Maxworthy, T. 1980*b* The nonlinear capillary instability of a liquid jet. Part 3. Experiments on satellite drop formation and control. *J. Fluid Mech.* **96**, 287–297.

Dias, F. & Vanden-Broeck, J.-M. 1990 Flows emerging from a nozzle and falling under gravity. *J. Fluid Mech.* **213**, 465–477.

Donnelly, R. J. & Glaberson, W. 1966 Experiments on the capillary instability of a liquid jet. *Proc. R. Soc. Lond.* A **290**, 547–556.

Eggers, J. 1997 Nonlinear dynamics and breakup of free-surface flows. *Rev. Mod. Phys.* **69**, 865–929.

Finnicum, D. S., Weinstein, S. J. & Ruschak, K. J. 1993 The effect of applied pressure on the shape of a two-dimensional liquid curtain falling under the influence of gravity. *J. Fluid Mech.* **255**, 647–665.

Goedde, E. F. & Yuen, M. C. 1970 Experiments on liquid jet instability. *J. Fluid Mech.* **40**, 495–511.

Hilbing, J. H., Heister, S. D. 1996 Droplet size control in liquid jet breakup. *Phys. Fluids* **8**, 1574–1581.

Keller, J. B. & Geer, J. 1973 Flows of thin streams with free boundaries. *J. Fluid Mech.* **59**, 417–432.

Keller, J. B., Rubinow, S. I. & Tu, Y. O. 1973 Spatial instability of a jet. *Phys. Fluids* **16**, 2052–2055.

Keller, J. B., Weitz, M. L. 1957 Upward 'falling' jets and surface tension. *J. Fluid Mech.* **2**, 201–203.

Middleman, S. 1995 *Modeling Axisymmetric Flows: Dynamics of Films, Jets, and Drops*. Academic.

Peregrine, D. H., Shoker, G. & Symon, A. 1990 The bifurcation of liquid bridges. *J. Fluid Mech.* **212**, 25–39.

Ramos, J. I. 1996 Upward and downward annular liquid jets: Conservation properties, singularities, and numerical errors. *Appl. Math. Modelling* **20**, 440–458.

Rayleigh, Lord 1878 On the instability of jets. *Proc. Lond. Math. Soc.* **10**, 4–13.

Schulkes, R. M. S. M. 1993 Dynamics of liquid jets revisited. *J. Fluid Mech.* **250**, 635–650.

Tuck, E. O. 1976 The shape of free jets of water under gravity. *J. Fluid Mech.* **76**, 625–640.

Wallwork, I. M. 2001 The trajectory and stability of a spiralling liquid jet. PhD thesis, The University of Birmingham.

Wallwork, I. M., Decent, S. P. & King, A. C. 2000 The trajectory and stability of a spiralling liquid jet. *Proc. IUTAM Symp. on Free Surface Flows, Birmingham, UK, 10–14 July 2000.*

Weber, C. 1931 Zum Zerfall eines Flussigkeitsstrahles. *Z. Angew. Math. Mech.* **1**, 136–141.